Global Biogeochemical Cycles®

RESEARCH ARTICLE
10.1029/2022GB007354

Key Points:

- Twenty-Five percentage of marine annual net community production (ANCP) accumulates as dissolved organic phosphorus (DOP) with a mean surface ocean lifetime of 0.5–2 years
- Autotrophic uptake of DOP supplies 14% of global ANCP with regional contributions as large as 80%
- Shallow subsurface DOP consumption and surface Ekman convergence create a shallow overturning loop retaining P within the ocean subtropics

Correspondence to:
R. T. Letscher,
robert.letscher@unh.edu

Citation:
Letscher, R. T., Wang, W.-L., Liang, Z., & Knapp, A. N. (2022). Regionally variable contribution of dissolved organic phosphorus to marine annual net community production. *Global Biogeochemical Cycles*, *36*, e2022GB007354. https://doi.org/10.1029/2022GB007354

Received 11 FEB 2022
Accepted 27 NOV 2022

Author Contributions:
Conceptualization: Robert T. Letscher, Angela N. Knapp
Formal analysis: Robert T. Letscher, Wei-Lei Wang, Angela N. Knapp
Funding acquisition: Robert T. Letscher, Angela N. Knapp
Methodology: Robert T. Letscher, Wei-Lei Wang
Project Administration: Robert T. Letscher, Angela N. Knapp
Resources: Robert T. Letscher
Software: Robert T. Letscher, Wei-Lei Wang
Validation: Robert T. Letscher
Visualization: Robert T. Letscher
Writing – original draft: Robert T. Letscher
Writing – review & editing: Robert T. Letscher, Wei-Lei Wang, Angela N. Knapp

Regionally Variable Contribution of Dissolved Organic Phosphorus to Marine Annual Net Community Production

Robert T. Letscher[1], Wei-Lei Wang[2], Zhou Liang[3], and Angela N. Knapp[3]

[1]Earth Sciences & Ocean Process Analysis Laboratory, University of New Hampshire, Durham, NH, USA, [2]State Key Lab of Marine Environmental Science, College of Ocean and Earth Sciences, Xiamen University, Xiamen, China, [3]Earth, Ocean, & Atmospheric Science, Florida State University, Tallahassee, FL, USA

Abstract Marine dissolved organic phosphorus (DOP) serves as an organic nutrient to marine autotrophs, sustaining a portion of annual net community production (ANCP). Numerical models of ocean circulation and biogeochemistry have diagnosed the magnitude of this process at regional to global scales but have thus far been validated against DOP observations concentrated within the Atlantic basin. Here we assimilate a new marine DOP data set with global coverage to optimize an inverse model of the ocean phosphorus cycle to investigate the regionally variable role of marine DOP utilization by autotrophs contributing to ANCP. We find ~25% of ANCP accumulates as DOP with a regionally variable pattern ranging from 8% to 50% across nine biomes investigated. Estimated mean surface ocean DOP lifetimes of ~0.5–2 years allow for transport of DOP from regions of net production to net consumption in subtropical gyres. Globally, DOP utilization by autotrophs sustains ~14% (0.9 Pg C yr^{-1}) of ANCP with regional contributions as large as ~75% within the oligotrophic North Atlantic and North Pacific. Shallow export and remineralization of DOP within the ocean subtropics contributes ~30%–80% of phosphate regeneration within the upper thermocline (<300 m). These shallow isopycnals beneath the subtropical gyres harboring the preponderance of remineralized DOP outcrop near the poleward edge of each gyre, which when combined with subsequent lateral transport equatorward by Ekman convergence, provide a shallow overturning loop retaining phosphorus within the subtropical biome, likely helping to sustain gyre ANCP over multiannual to decadal timescales.

Plain Language Summary Marine phytoplankton require nitrogen (N) and phosphorus (P) nutrients to sustain growth. Over large regions of the global ocean, concentrated at subtropical latitudes, supply of inorganic N and P is greatly diminished yet these regions are observed to sustain phytoplankton growth and the export of the organic matter they produce to intermediate ocean depths. Here, we investigate the role for the alternative P pool, dissolved organic phosphorus, to sustain marine phytoplankton growth and find that regionally it may contribute up to 75% of the required P in the subtropical North Atlantic and North Pacific, averaging 14% for the global ocean.

1. Introduction

Dissolved phosphorus (P) has long been recognized as a globally important "macro"-nutrient that can limit marine biological productivity across various spatial and temporal scales. Decades of research have focused on the biogeochemical cycling and availability of dissolved inorganic phosphorus in seawater, dominated by the phosphate ion (PO_4^{3-}) and its associated protonated forms, to both infer and predict spatiotemporal patterns of marine biomass production and its subsequent turnover by heterotrophic microbes. However, in recent years other pools of P present in seawater have increasingly gained appreciation as potential sources of P supporting marine biological productivity including inorganic polyphosphate (Diaz et al., 2018; P. Martin et al., 2014; Orchard, Benitez-Nelson, et al., 2010) and organic phosphorus-containing esters (e.g., Mather et al., 2008; Orchard, Ammerman, et al., 2010; Reynolds et al., 2014), and phosphonates (Dyhrman et al., 2006), collectively termed dissolved organic phosphorus (DOP). Many major lineages of marine phytoplankton are known to harbor enzymes capable of accessing these organic forms of P including cyanobacteria (Dyhrman et al., 2006; Su et al., 2007), diatoms (Lin et al., 2013), and other eukaryotic algae (Li et al., 2018; Shaked et al., 2006), with numerous field and laboratory studies having documented the ability of these algal taxa to use DOP to supplement and/or satisfy their cellular P requirements (e.g., Björkman & Karl, 2003; Dyhrman & Ruttenberg, 2006; Orchard, Ammerman, et al., 2010).

Near surface waters (<150 m) of subtropical oceans (~10°–40°) perennially exhibit low concentrations of PO_4^{3-}, typically on the order of ~10–300 nM (Martiny et al., 2019), with similarly depleted concentrations of nitrate (Eppley et al., 1990). This macronutrient limitation of net primary production (NPP) results in the global minima of vertically integrated annual NPP rates found in the subtropical ocean (Behrenfeld & Falkowski, 1997; Behrenfeld et al., 2005). The related biogeochemical flux, net community production (NCP), represents the amount of organic matter fixed in excess of total community energy requirements, typically evaluated over annual timescales, and is supported by exogenous inputs of nutrients into the productive euphotic zone (Dugdale & Goering, 1967; Eppley & Peterson, 1979). The estimated subtropical to extratropical NCP gradient is less variable than for NPP (Emerson, 2014); however, there is a longstanding conundrum in ocean biogeochemistry to explain subtropical ocean NCP rates given estimates of the exogenous inorganic nutrient inputs at these latitudes (Gruber et al., 1998; Johnson et al., 2010; Keeling et al., 2004; Michaels et al., 1994).

Lateral supply of organic nutrients including DOP and dissolved organic nitrogen (DON) to gyres from the more productive equatorial, eastern, and poleward boundaries have been suggested to supplement subtropical ocean nutrient budgets (Charria et al., 2008; Letscher et al., 2016; Reynolds et al., 2014; Roussenov et al., 2006; Torres-Valdés et al., 2009), with additional heterotrophic and/or autotrophic processing of the organic macromolecules involved to liberate bioavailable P and N. This process is best characterized for the North Atlantic subtropical gyre where surface PO_4^{3-} concentrations are at or near the global minima (~1–10 nM, Martiny et al., 2019; Wu et al., 2000), leading to P limitation of NPP and NCP (Ammerman et al., 2003; Lomas et al., 2010), for which lateral supply of DOP may provide a nutritional subsidy to marine phytoplankton (Duhamel et al., 2021; Reynolds et al., 2014). Mather et al. (2008) reported on the latitudinal and longitudinal gradients in DOP, PO_4^{3-}, and alkaline phosphatase activity (APA), a common enzyme used by marine plankton to access P in DOP across the Atlantic basin, finding strong observational support for the microbial utilization of surface ocean DOP when surface PO_4^{3-} dropped below ~100–200 nM. Many other field studies have documented the ability of individual phytoplankton taxa and the community to utilize DOP as a P source sustaining growth across the North Atlantic and North Pacific subtropical gyres (Björkman & Karl, 2003; Casey et al., 2009; Lomas et al., 2010; Orchard, Ammerman, et al., 2010).

To date, regional estimates of the role for lateral DOP supply in sustaining subtropical ocean NCP have come from ocean biogeochemistry/ecosystem models coupled with ocean circulation models that have represented marine DOP cycling, including its utilization by autotrophs. These models suggest that on the order of 30%–70% of NCP in the subtropical North Atlantic is supported by the lateral, exogenous supply of DOP from the gyre margins (Reynolds et al., 2014; Roussenov et al., 2006; Torres-Valdés et al., 2009). A global modeling study extended estimates for the fraction of subtropical NCP supported by lateral DOP utilization to all subtropical gyre regions, corroborating the particular importance of this process within the North Atlantic (~43% of P needed to explain NCP), while finding a reduced but still significant role for DOP, ranging from 19% to 31% of the P supply for the South Atlantic, Pacific, and Indian Ocean subtropical gyres (Letscher et al., 2016). It should be noted that the representation of the marine DOP cycle in all the above modeling studies was validated against an observational DOP concentration database that was largely limited to the Atlantic Ocean, especially the North Atlantic prior to 2015 (Letscher & Moore, 2015). The meridional and zonal gradients in surface ocean DOP concentrations outside of the Atlantic basin are largely unknown except for a handful of studies from the Pacific (Abell et al., 2000; Hashihama et al., 2020; Lanpher & Popendorf, 2021; Moutin et al., 2008; Yoshimura et al., 2007). These observed DOP gradients in the subtropical Pacific generally support the proposed mechanism of lateral DOP supply from the productive margins supporting a portion of NCP in the gyres; however, a basin- to regional-scale analysis of DOP support of NCP within the Pacific and Indian Oceans, calibrated against a large-scale characterization of DOP concentrations in these basins, is currently lacking.

Here, we make use of recently compiled DOP concentration data for the open ocean, the DOPv2021 database (Knapp et al., 2021), which has doubled the number of DOP observations compared to its predecessor (Letscher & Moore, 2015), with improved spatial coverage of the Pacific basin and some coverage of the Indian basin for the first time. The new DOP database is used to more accurately assess the importance of DOP cycling for sustaining a portion of NCP within a regional context while also providing the first global estimates of this important biogeochemical flux by inclusion of extra-subtropical regions. The DOP observational data are assimilated into an inverse model of the marine P-cycle coupled to a representation of the contemporary ocean circulation to diagnose the annual biogeochemical fluxes of the marine DOP cycle at steady state, for example, accumulation from biological productivity, heterotrophic remineralization, and autotrophic utilization, that are most consistent

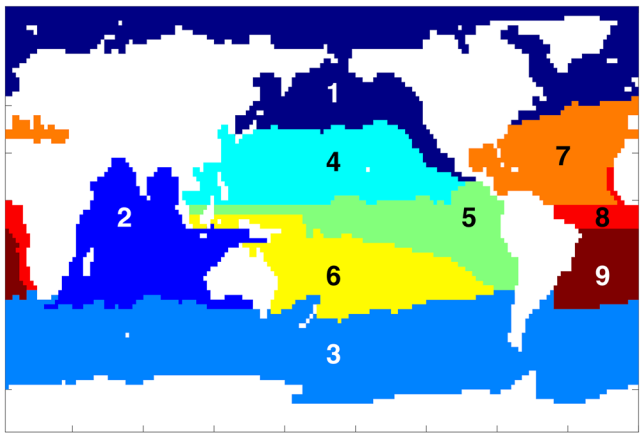

Figure 1. Nine unique biogeochemical regions separated by surface ocean phosphate concentrations above or below 0.3 μM. Region 1 = Northern; 2 = Indian; 3 = Southern; 4 = North Pacific subtropical gyre; 5 = equatorial Pacific; 6 = South Pacific subtropical gyre; 7 = North Atlantic subtropical gyre; 8 = equatorial Atlantic; and 9 = South Atlantic subtropical gyre.

with the spatial and vertical gradients observed for DOP. Output from the inverse model is then used to quantify the regionally variable pattern of DOP-supported NCP across the global ocean. Model output is also used to identify and quantify the spatial pattern of exported DOP below the productive layer as it is regenerated within the shallow surfaces of the ocean interior.

2. Methods

2.1. Model Design

This study builds on the equilibrium, steady-state P-cycling model of Wang et al. (2019) that was used to diagnose spatial patterns in marine nitrogen fixation rates. The model couples a representation of the time-mean ocean circulation in the form of a tracer transport matrix, the Ocean Circulation Inverse Model v2 (OCIM2, DeVries & Holzer, 2019), with a parameterization of the marine biogeochemical fluxes of P, which we term the OCIM P-cycling model. The OCIM2 is a data-constrained ocean circulation model that assimilates observational tracers to estimate the climatological mean (steady state) circulation and has been employed in numerous biogeochemical studies (e.g., DeVries & Deutsch, 2014; DeVries et al., 2013; John et al., 2020; Weber et al., 2016). The OCIM P-cycling model used here predicts 3D distributions of dissolved inorganic phosphorus (DIP) (i.e., PO_4^{3-} but we use DIP to differentiate model predicted phosphate from observed PO_4^{3-}), particulate organic phosphorus (POP), and "semilabile" DOP (lifetime ~months to years) representative of the time-mean conditions for the contemporary ocean. The version of the model employed in this study improves the representation of the marine DOP cycle by adding a term for autotrophic DOP utilization in the upper ocean while also assimilating observations of marine DOP concentration. Assimilation of observed DOP and PO_4^{3-} concentrations is used to objectively constrain a suite of tunable parameters that govern the representation of annual NCP (ANCP), the remineralization of its exported products, and specifically the sources and sinks of DOP within the global marine P-cycle.

The ~200,000 ocean grid boxes within the OCIM2 model grid are divided into nine biogeochemical regions (Figure 1) to find the spatially variable set of tunable parameters which optimize the representation of marine DOP cycling regionally across the global ocean. There are several a priori reasons why DOP cycling might differ across biogeochemical gradients including the well-documented P-limitation of the North Atlantic subtropical gyre relative to other basins (Ammerman et al., 2003); the observed zonal and meridional gradients in field-measured alkaline phosphatase enzyme activity across the Atlantic basin (Mather et al., 2008; Reynolds et al., 2014), and similar meridional gradients found for marine DOC cycling (e.g., Roshan & DeVries, 2017). The nine biogeochemical regions are defined using the 0.3 μM surface PO_4^{3-} concentration isoline from the World Ocean Atlas climatology to separate surface ocean nutrient-depleted and -replete regimes within each of the major ocean basins. The choice of nine regions was selected after also considering the distribution of DOP observational data to allocate the available data approximately evenly across regions (n = ~375–465 per region). Additional regional configurations were tested with 3–8 regions, which separated out increasingly smaller portions of the ocean (e.g., three regions = Atlantic, Pacific, rest of ocean and four regions = Atlantic, Pacific, Indian, rest of ocean, etc.). The optimized values obtained for the regionally variable parameters exhibited variability on the order of ~5%–20%. Globally integrated metrics such as ANCP rate and the fraction of ANCP supported by DOP presented in the Discussion varied by <9% across the suite of regional configurations.

2.2. Data Sets

Climatological mean concentrations of observed PO_4^{3-} concentration ($[PO4]_{obs}$) from the World Ocean Atlas 2013 climatology (Garcia et al., 2013) at a resolution of 1° lon × 1° lat × 33 vertical layers were triangularly interpolated onto the OCIM2 model grid at 2° lon × 2° lat × 24 vertical-layer resolution (36.1 m at z = 1 increasing to 663.5 m at z = 24). A recent global compilation of DOP concentration ([DOP]) measurements (the DOPv2021 database, Knapp et al., 2021) is similarly interpolated onto the OCIM2 model grid. The [DOP] database contains ~3,800 observations spanning the major global ocean basins except for the Arctic, with 97% of observations

located in the upper 1,000 m of the water column. For the OCIM P-cycling model we simulate "semilabile" DOP (defined in Section 2.3), for which we subtract a refractory DOP value of 0.05 μM, the asymptotic deep ocean (>1,000 m) [DOP] found in DOPv2021, from all DOP data in DOPv2021 to obtain observed, semilabile [DOP].

2.3. Model Equations and Tunable Parameters

The governing time tendency mass balance equations for [DIP], [DOP], and [POP] are as follows:

$$\frac{d[\mathrm{DIP}]}{dt} + \mathbf{T}[\mathrm{DIP}] = -\gamma[\mathrm{DIP}] + \kappa_d[\mathrm{DOP}] + \kappa_p[\mathrm{POP}] + \kappa_g\left([\mathrm{DIP}] - \overline{[\mathrm{PO4}]}_{\mathrm{obs}}\right), \tag{1}$$

$$\frac{d[\mathrm{DOP}]}{dt} + \mathbf{T}[\mathrm{DOP}] = \sigma\gamma[\mathrm{DIP}] - \kappa_d[\mathrm{DOP}] - \mu[\mathrm{DOP}], \tag{2}$$

$$\frac{d[\mathrm{POP}]}{dt} + \mathbf{F}[\mathrm{POP}] = (1-\sigma)\gamma[\mathrm{DIP}] - \kappa_p[\mathrm{POP}] + \mu[\mathrm{DOP}]. \tag{3}$$

The sources of DIP include from the heterotrophic remineralization of DOP and POP scaled by rate constants k_d and k_p, respectively, and the primary sink is autotrophic uptake scaled by a parameter, γ, which is applied to the top two vertical layers of the model (0–73 m), corresponding to the OCIM model's euphotic zone. The parameter k_p, governing the remineralization rate of POP, is not well constrained by the PO_4^{3-} distribution alone and is a prescribed value $(30\ \mathrm{d})^{-1}$ (Wang et al., 2019); k_d is a tunable parameter in the model with units = yr^{-1}. Sensitivity tests for k_p values of $(20\ \mathrm{d})^{-1}$ and $(40\ \mathrm{d})^{-1}$ were found to have no impact on the obtained tunable parameters. Gamma (γ) takes the functional form with respect to grid location ($\mathbf{r}$):

$$\gamma(\mathbf{r}) \equiv \begin{cases} \alpha \dfrac{\left[\dfrac{1}{r_{\mathrm{C:P}}}\dfrac{\mathrm{NPP}(\mathbf{r})}{\mathrm{NPP}_0}\right]^{\beta}}{\dfrac{[\mathrm{PO4}]_{\mathrm{obs}}(\mathbf{r})}{[\mathrm{PO4}]_{\mathrm{obs}_0}}}, & \text{if } z < z_c, \\ 0, & \text{otherwise}, \end{cases} \tag{4}$$

where α (units = s^{-1}) and β (unitless) are two tunable parameters to model the autotrophic biological uptake rate of DIP after considering information on the spatial distribution of marine NPP and upper ocean $[\mathrm{PO4}]_{\mathrm{obs}}$ gradients and has been used in previous versions of the OCIM P-cycling model (Primeau et al., 2013; Teng et al., 2014; Wang et al., 2019). The input field of vertically integrated, annual marine net primary productivity, NPP($\mathbf{r}$), is taken from the output of the Carbon-based Productivity Model using the SeaWiFS ocean color climatology (Behrenfeld et al., 2005) and converted to P units using a variable phosphorus to carbon ratio for marine particle production ($r_{\mathrm{C:P}}$) as a linear function of in situ $[\mathrm{PO4}]_{\mathrm{obs}}(\mathbf{r})$ concentrations (Galbraith & Martiny, 2015) in the World Ocean Atlas climatology. Biological uptake of DIP occurs when $z < z_c$, where $z_c = 73$ m, corresponding to the model's euphotic zone, and set to zero below. NPP_0 and $[\mathrm{PO4}]_{\mathrm{obs0}}$ are equivalent to 1 mmol C $\mathrm{m}^{-2}\ \mathrm{s}^{-1}$ and 1 mmol m^{-3}, respectively, to ensure that the dimensions of γ are s^{-1}. The total ocean inventory of P is conserved in our equilibrium simulations by inclusion of a small source of DIP with a restoring timescale of $k_g = (10^6\ \mathrm{yr})^{-1}$ back to the global mean observed $[\mathrm{PO4}]_{\mathrm{obs}} = 2.1$ μM to account for the small loss of P from the model domain when POP reaches the seafloor.

Owing to a general lack of knowledge about the sources and sinks of the refractory (lifetime ~centuries to millennia) fraction of marine DOP, we have chosen to simulate nonrefractory, "semilabile," marine DOP which is thought to cycle on monthly to yearly timescales (Karl & Björkman, 2015), while also ignoring "labile" DOP which cycles on ~hourly timescales. The source of semilabile DOP in the model is as a uniform fraction, σ (a tunable parameter), of autotrophic production of organic matter (γ[DIP]). The two sinks for semilabile DOP include heterotrophic remineralization with rate constant k_d that occurs throughout the model domain and autotrophic uptake of DOP with rate constant μ, which is applied in the upper two vertical layers of the model. μ takes the form of the reciprocal of the Monod equation:

$$\mu = \upsilon \frac{K_s + [\mathrm{PO4}]_{\mathrm{obs}}}{[\mathrm{PO4}]_{\mathrm{obs}}}, \tag{5}$$

where v is the minimum semilabile DOP uptake rate (units = yr^{-1}) at elevated in situ concentrations of $[PO4]_{obs}$ and K_s (units = μM) is a tunable parameter describing the half-saturation constant for maximal DOP uptake rates at low $[PO4]_{obs}$. Initial simulations with both v and K_s as tunable parameters revealed a large covariance inhibiting the ability to constrain both parameters within acceptable levels of uncertainty. We therefore prescribed $v = 0.05\ yr^{-1}$, the approximate minimum DOP uptake rates observed in extant field studies (Mather et al., 2008; Reynolds et al., 2014; Sato et al., 2013). Sensitivity tests for v values of 0.1 and 0.033 yr^{-1} were found to have a minor impact (<±5%) on the obtained tunable parameters, with the most significant effect observed for the optimized σ values (<±20%).

The production of POP in the model is from the fraction $(1 - \sigma)$ of autotrophic DIP uptake (γ[DIP]) and from the autotrophic uptake of DOP, μ[DOP]. Loss of POP below the surface productive layer (at depths >73 m) occurs at the timescale of $k_p = (30\ d)^{-1}$. **T** is the advection (**u**) and diffusion (**K**) operator for tracer ([C]) transport defined as $\mathbf{T}[C] = \nabla\cdot(\mathbf{u}[C] - \mathbf{K}\nabla[C])$ taken from the output of the OCIM2 expressed as a tracer transport matrix. **F** is the vertical flux divergence operator defined as follows:

$$\mathbf{F} = (1-\sigma)\left[\frac{d}{dz}\left(\frac{z}{z_{73m}}\right)^{-b}\right]\int_{z_{73m}}^{0}(\gamma[DIP] + \mu[DOP])dz, \tag{6}$$

where the vertically integrated flux of POP production from the sum of DIP and DOP uptake above 73 m is attenuated with depth following a power law function fit with the tunable parameter, b.

In summary, the OCIM P-cycling model assimilates observational PO_4^{3-} and DOP data to constrain a set of tunable parameters; σ, k_d, K_s, α, β, and b; yielding prognostic estimates of the 3D distribution of [DIP], [DOP], and [POP] for the contemporary, steady-state ocean. A unique σ, k_d, and K_s are found for each of the nine biogeochemical regions with a single global value for α, β, and b; thus the total number of tunable parameters is 30.

2.4. Model Simulations

Assuming the modern marine P cycle is at steady state, the time tendency terms in Equations 1–3 disappear and the system of three linear algebraic equations can be solved using direct matrix inversion carried out in Matlab® software. The solution to each equation yields the prognostic 3D distribution of [DIP], [DOP], and [POP] as an implicit function of the model's tunable parameters. The set of tunable parameters, which we define as θ, are optimized using a Bayesian method that minimizes the negative of the log posterior of the likelihood function to estimate the most probable parameter values conditioned on the assimilated PO_4^{3-} and DOP observational data. At the core of the likelihood function is the computed error, e, between model-predicted and observed tracer concentrations for both DIP and DOP, which we assume are normally and independently distributed:

$$e_{[DIP],i} = \frac{[DIP]_i(\theta) - [PO4]_{obs}}{S_{DIP,i}},\ \text{for } i = 1\ldots n_{Pi}, \tag{7}$$

$$e_{[DOP],i} = \frac{[DOP]_i(\theta) - [DOP]_{obs}}{S_{DOP,i}},\ \text{for } i = 1\ldots n_{Po}, \tag{8}$$

where $[PO4]_{obs}$ and $[DOP]_{obs}$ are the observed concentrations of PO_4^{3-} and semilabile DOP (total DOP–0.05 μM) from the World Ocean Atlas and DOPv2021 databases, respectively, S_{DIP} and S_{DOP} are the standard deviations of all available observations of each, and n_{Pi} and n_{Po} are the number of independent DIP and DOP observation-model output pairs in the model design. The likelihood function also considers the assigned weighting to the assimilated data, W_{Pi} and W_{Po}, which is computed as the fraction of volume ($V_i/\Sigma V$) at each grid point multiplied by the variance of the DIP and DOP observational data, respectively. The negative of the log-likelihood function is thus:

$$L(\theta) = \frac{1}{2}\left(e'_{[DIP]}W_{Pi}e_{[DIP]}\right) + \frac{1}{2}\left(e'_{[DOP]}W_{Po}e_{[DOP]}\right). \tag{9}$$

The function (Equation 9) is minimized to find the most probable values of the tunable parameters within θ, using the optimization algorithm provided by Matlab®'s fminunc function. To perform efficiently, the algorithm relies on both the gradient, $\nabla_\theta L$, and the Hessian, $\nabla_{\theta\theta} L$, of the log posterior with respect to the parameters (Equation 9),

Table 1
The Optimized Parameter Values, Collectively "θ," Including the Upper Bound (e^+) and Lower Bound (e^-) Estimates of the Uncertainty

Region	ID	Parameter	Value	e^+	e^-
Northern	1	σ	0.495	0.030	0.030
Indian	2	σ	0.080	0.003	0.003
Southern	3	σ	0.183	0.004	0.004
NPSG	4	σ	0.253	0.005	0.005
EqPac	5	σ	0.264	0.008	0.008
SPSG	6	σ	0.249	0.017	0.017
NASG	7	σ	0.121	0.008	0.008
EqAtl	8	σ	0.100	0.011	0.010
SASG	9	σ	0.122	0.012	0.011
Northern	1	$(k_d)^{-1}$	2.032	0.080	0.080
Indian	2	$(k_d)^{-1}$	3.807	0.640	0.548
Southern	3	$(k_d)^{-1}$	9.748	0.412	0.396
NPSG	4	$(k_d)^{-1}$	3.048	0.085	0.085
EqPac	5	$(k_d)^{-1}$	4.711	0.227	0.217
SPSG	6	$(k_d)^{-1}$	4.555	0.167	0.161
NASG	7	$(k_d)^{-1}$	4.109	0.392	0.358
EqAtl	8	$(k_d)^{-1}$	3.660	0.791	0.650
SASG	9	$(k_d)^{-1}$	4.308	0.323	0.300
Northern	1	K_s	0.188	0.017	0.016
Indian	2	K_s	0.205	0.009	0.009
Southern	3	K_s	0.208	0.051	0.051
NPSG	4	K_s	0.179	0.019	0.017
EqPac	5	K_s	0.201	0.020	0.020
SPSG	6	K_s	0.187	0.021	0.019
NASG	7	K_s	0.192	0.047	0.038
EqAtl	8	K_s	0.206	0.014	0.014
SASG	9	K_s	0.195	0.013	0.008
		α	1.66×10^{-4}	9.25×10^{-7}	9.20×10^{-7}
		β	0.0259	0.0006	0.0006
		b	1.186	0.0014	0.0014

Note. Units: σ = unitless; $(k_d)^{-1}$ = yr; K_s = μM; α = s^{-1}; β = unitless; and b = unitless.

which were coded by hand. Initial values for θ were taken from the global best fit solutions to the previous version of the OCIM P-cycling model (Wang et al., 2019). The optimization generally converged after 30 iterations.

We estimate the uncertainty on each tunable parameter within θ by approximating the posterior probability using a Gaussian centered at θ_p, the most probable values of θ. The posterior covariance matrix for θ_p is given by the following equation:

$$\Sigma = \langle (\theta - \theta_p)(\theta - \theta_p)' \rangle \approx -\left[\nabla_{\theta\theta} L|_{\theta=\theta_p}\right]^{-1}. \quad (10)$$

All error bars on the parameter values within θ reported in Table 1 represent ±1 standard deviation of the posterior after marginalizing out all but the parameter of interest. They are obtained from the square root of the diagonal elements of Σ.

3. Results

3.1. Tunable Parameters

The most probable values of the 30 tunable parameters within θ_p are presented in Table 1 along with their estimated upper bound (e^+) and lower bound (e^-) uncertainty. Parameter σ, the fraction of P-based NCP that accumulates as semilabile DOP in the productive layer, ranged from 0.08 to 0.50. Accumulating fractions in the three regions covering the Atlantic basin were statistically indistinguishable from each other with a value of ~0.114 ± 0.01. A slightly lower value of σ = 0.080 ± 0.003 was found for the Indian Ocean region. Accumulating fractions of DOP were higher in the Pacific Ocean regions, in the narrow range σ = 0.240–0.264. The highest value of σ was found for the northern region, σ = 0.495 ± 0.03. The Southern Ocean exhibited σ = 0.183 ± 0.004, intermediate between the Atlantic and Pacific Ocean regions. The relative uncertainty on the nine estimated values of σ is low, ranging from ~2%–11%; mean 5.5%.

Parameter k_d represents the heterotrophic remineralization rate of semilabile DOP and has units of yr^{-1}. The inverse of k_d is presented in Table 1, representing the heterotrophic remineralization e-folding timescale expressed in units of years. Timescales for heterotrophic semilabile DOP consumption ranged between 2.0 and 9.7 yr. There is no distinguishable difference in heterotrophic DOP consumption timescales between the Atlantic and Pacific basins which averaged 4.1 ± 0.6 yr across the six relevant regions. Interestingly, the northern and southern regions exhibited the minimum and maximum DOP consumption timescales at 2.0 ± 0.1 and 9.8 ± 0.4 yr, respectively. Relative uncertainty on the estimated values of k_d is slightly higher, ranging from ~3% to 22%; mean = ~7.9%. The globally averaged, mean heterotrophic remineralization timescale of semilabile DOP is 3.8 ± 0.9 yr. Parameter K_s represents the half-saturation constant governing the autotrophic uptake rate of semilabile DOP within the productive layer. The most probable values of K_s fell into the narrow range of 0.179–0.208 ± 0.01 μM (Table 1). Relative uncertainty on the estimated K_s values ranged from ~4% to 24%; mean 11.3%.

The most probable values of the globally fit constants α, β, and b are presented in Table 1. Parameters α and β, fitting constants for modeling autotrophic DIP uptake while accounting for the spatial pattern of marine NPP, were estimated at values of $\alpha = 1.66 \times 10^{-4} \pm 9.2 \times 10^{-7}$ s^{-1} and β = 0.0259 ± 0.0006, representing a relative uncertainty of 0.55% and 2.4%, respectively. Parameter b, the exponent governing POP flux attenuation with depth, was found to have a most probable value of 1.186 ± 0.001, with a low relative uncertainty of 0.12%. The larger estimated value of b found here as compared to the canonical Martin's b exponent (b = 0.858, J. H. Martin

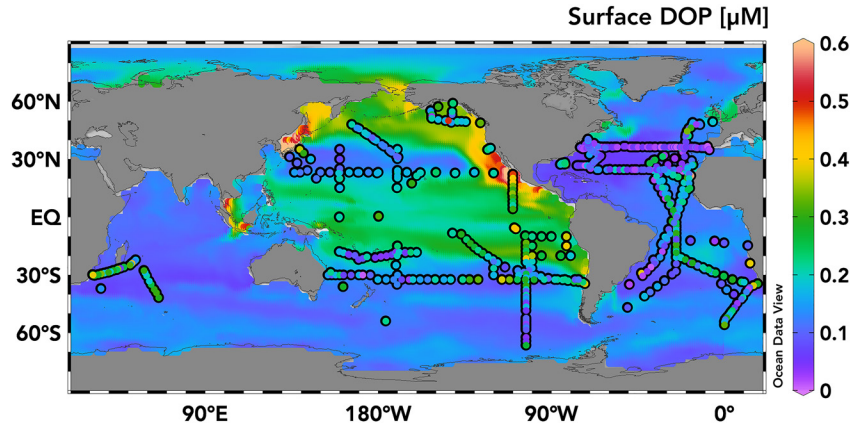

Figure 2. Surface ocean bulk dissolved organic phosphorus concentration ([DOP]) (μM) predicted by the OCIM P-cycling model output (color mapping), overlain with observations of [DOP] from the DOPv2021 database (Knapp et al., 2021) (colored circles).

et al., 1987) expressed in terms of POC flux attenuation represents a more rapid attenuation of POP with depth diagnosed by the OCIM P-cycling model.

3.2. [DOP]

The steady-state surface ocean concentration of total [DOP] (simulated semilabile [DOP] + uniform 0.05 μM refractory [DOP]) averaged over the productive layer (0–73 m) from the OCIM P-cycling model (color mapping) and the [DOP] observations from the DOPv2021 database (colored dots) are presented in Figure 2. Modeled surface ocean [DOP] ranges from 0.03 to 0.6 μM, with a global mean value of 0.16 ± 0.08 μM (±1 S.D.). The model output and observations both identify the global open ocean maximum in [DOP] = ~0.5–0.6 μM within the eastern subtropical to tropical Pacific (regions 1, 4, and 5), largely corresponding to the known regions of eastern boundary upwelling and/or elevated iron stress. The model predicts intermediate [DOP] (~0.25–0.4 μM) within the subarctic North Pacific (region 1) that are overestimated relative to the observations (Figure 2). Intermediate modeled [DOP] are also found between ~20°N and 20°S across the Pacific Ocean (~0.25–0.4 μM; regions 4, 5, and 6) and within a similar latitude range in the Atlantic Ocean (regions 7–9), albeit at lower concentrations (~0.15–0.2 μM). Both the model and observations identify the global open ocean minimum in [DOP] = ~0.03–0.05 μM to lie within the North Atlantic subtropical gyre, especially the western half (Sargasso Sea), which has been well documented (Lomas et al., 2010; Mather et al., 2008; Reynolds et al., 2014; Torres-Valdés et al., 2009). Modeled surface [DOP] is ~0.1–0.25 μM within the polar seas of the Arctic (region 1) and Southern Oceans (region 3). A global ocean and full-depth, pointwise comparison of modeled versus observed [DOP] yielded a correlation coefficient, $r = 0.54$, a root mean square error of 0.058 μM, and an overall negative mean bias of ~−4%. The latter metric implies that the model output underpredicts [DOP] by 4% compared against observations globally; however, the variance between comparisons was normally distributed with no systemic regional biases observed.

3.3. DOP Source/Sink

The annual, vertically integrated semilabile DOP production flux (mol P m^{-2} yr^{-1}) within the upper 73 m is presented in Figure 3a. Semilabile DOP is produced at elevated rates, ~0.015–0.03 mol P m^{-2} yr^{-1}, within the Pacific basin eastern boundary upwelling systems (regions 1 and 5) and the midlatitude to subarctic North Pacific and North Atlantic basins (region 1). The semilabile DOP production flux is similarly elevated within the eastern tropical South Pacific in the region between ~10 and 20°S and extending west to ~140°W (region 5). Within the Atlantic, DOP production fluxes are similarly elevated on the eastern side of the basins (regions 7 and 9), approaching rates of 0.01 mol P m^{-2} yr^{-1}. DOP production fluxes are at a minimum within the subtropical gyre regions of each basin (regions 2, 4, 6, 7, and 9), exhibiting the range ~0.0005–0.003 mol P m^{-2} yr^{-1}. The annual, vertically integrated autotrophic uptake rate of semilabile DOP [mmol P m^{-2} yr^{-1}] within the upper 73 m is

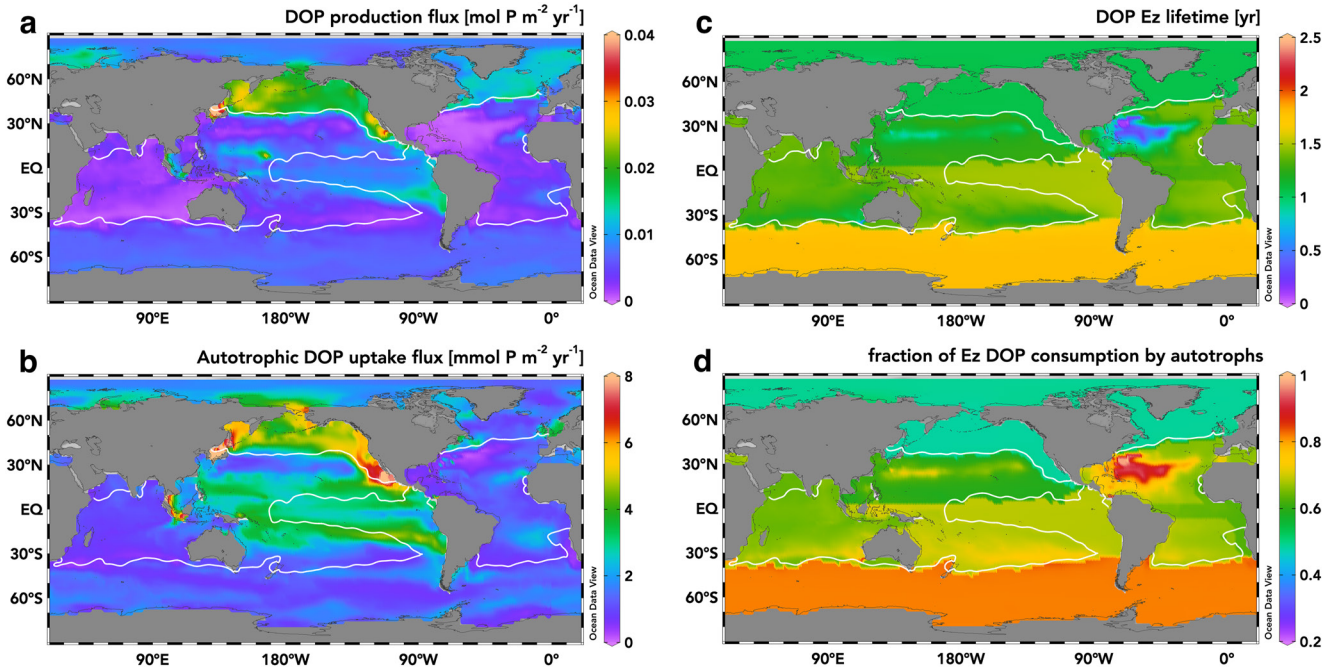

Figure 3. Autotrophic sources and sinks contributing to the mean lifetime of semilabile dissolved organic phosphorus (DOP) within the euphotic zone (Ez = 0–73 m). (a) Ez vertically integrated semilabile DOP production flux in mol P m^{-2} yr^{-1}. (b) Ez vertically integrated autotrophic semilabile DOP uptake flux in mmol P m^{-2} yr^{-1}. (c) Mean lifetime of semilabile DOP (yr) within the Ez resulting from the combination of autotrophic DOP production, autotrophic and heterotrophic DOP consumption, and ocean circulation. (d) Fraction of semilabile DOP consumption within the Ez contributed by autotrophic DOP uptake; remainder contributed by heterotrophic DOP remineralization. White isoline is the surface ocean $[PO4]_{obs}$ = 0.3 μM contour from the World Ocean Atlas.

presented in Figure 3b. Autotrophic semilabile DOP utilization ranges from ~0.5–8 mmol P m^{-2} yr^{-1} with lower values typically found in the Southern Ocean and within the western half of the subtropical gyres of each basin (regions 2, 4, 7, and 9) except for the South Pacific subtropical gyre. Elevated autotrophic DOP utilization rates are found within, and immediately "downstream" of, the productive ecosystems that border the subtropical gyres: the eastern boundary and tropical upwelling regions (regions 1, 5, 8, and 9) as well as the subtropical to midlatitude transition zone (regions 1 and 3). The Pacific basin exhibits overall higher rates than the Atlantic basin. Autotrophic DOP uptake is elevated in the Sea of Japan in the western Pacific (region 1) that may be an artifact of not well-represented ocean circulation in this semienclosed basin at the 2° spatial resolution of the OCIM model affecting nutrient supply to the Sea. The combined result of the semilabile DOP source minus sink fluxes within the productive layer (DOP production minus combined autotrophic + heterotrophic DOP consumption) coupled with the DOP upper ocean stock are used to calculate the mean lifetime of semilabile DOP within the model euphotic zone (upper 73 m, Figure 3c). Semilabile DOP lifetimes are shortest within the North Atlantic subtropical gyre (<1 yr) and longest within the Southern Ocean (~1.8 yr). Within each major ocean basin, semilabile DOP lifetimes are shortest within the subtropical gyres, on the order of ~0.75–1.25 yr (regions 2, 4, 6, 7, and 9). The fraction of combined autotrophic and heterotrophic DOP consumption within the euphotic zone attributable to autotrophic DOP uptake is presented in Figure 3d. Autotrophs contribute the preponderance (>0.5) of euphotic zone DOP consumption globally, with maximal contributions (~0.75–0.90) found for the North Atlantic subtropical gyre (especially the Sargasso Sea) and South Atlantic subtropical gyre, North Pacific and South Pacific subtropical gyres, and the Southern Ocean.

3.4. New Production

Vertically integrated, ANCP rates in phosphorus units (mol P m^{-2} yr^{-1}) computed from the sum of autotrophic DIP (γ[DIP]) and DOP (μ[DOP]) uptake minus POP (k_p[POP]) and DOP (k_d[DOP]) regeneration occurring within the euphotic zone is presented in Figure 4a. ANCP rates are elevated, ~0.02–0.04 mol P m^{-2} yr^{-1}, within the subarctic North Pacific and Atlantic (region 1), Southern Ocean, eastern boundary and Arabian Sea upwelling regions (regions 1, 2, 5, 7, and 9), and across the equatorial Pacific. Minima are found within the subtropical

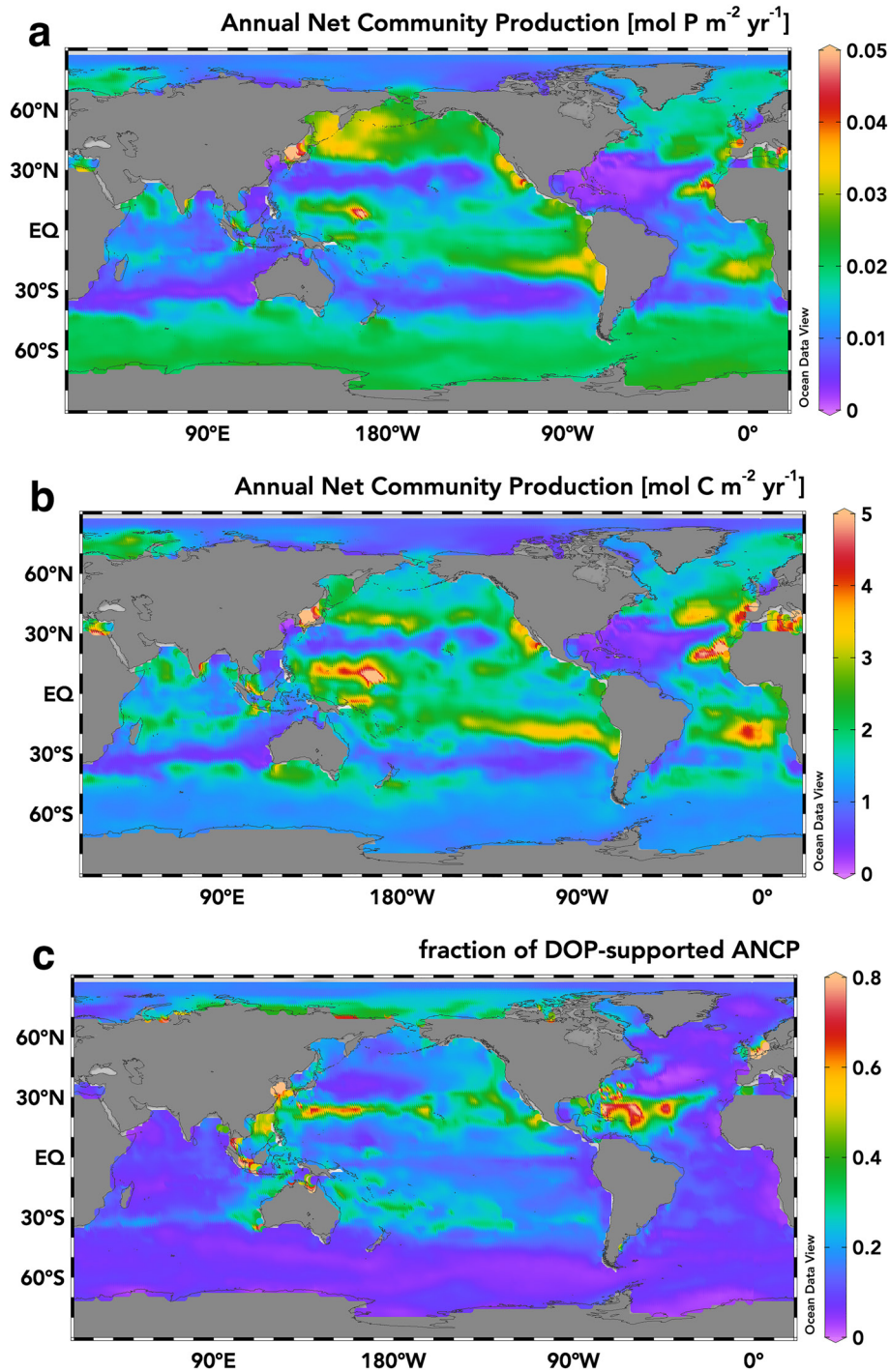

Figure 4. (a) OCIM P-cycling model predicted annual net community production (ANCP) rates in phosphorus units, mol P m^{-2} yr^{-1}. (b) ANCP rates in carbon units, mol C m^{-2} yr^{-1}, applying the regionally variable $r_{C:P}$. (c) The fraction of ANCP supported by autotrophic uptake of dissolved organic phosphorus.

gyres (regions 2, 4, 6, 7, and 9) and Arctic (region 1) in the range ~0.005–0.015 mol P m^{-2} yr^{-1}. Regionally averaged ANCP rates range by a factor of ~2 from 9.9 to 20.2 mmol P m^{-2} yr^{-1} (Table 2). ANCP rates converted to carbon units (mol C m^{-2} yr^{-1}) using the regionally variable $r_{C:P}$ based on in situ $[PO4]_{obs}$ (Galbraith & Martiny, 2015) is presented in Figure 4b. Carbon-based ANCP rates are maximal within eastern boundary upwelling systems (regions 1, 5, 7, and 9) and their immediately adjacent "downstream" regions in the range of

Table 2
Regional Contributions to Annual Net Community Production (ANCP) Rates in (mmol P m^{-2} yr^{-1}), (Pg C yr^{-1}), Regional % of Global ANCP, Dissolved Organic Phosphorus (DOP)-Supported ANCP (Pg C yr^{-1}), and Regional % of ANCP Supported by DOP

Region	ID	ANCP (mmol P m^{-2} yr^{-1})	ANCP (Pg C yr^{-1})	Regional % of global ANCP (%)	ANCP-DOP (Pg C yr^{-1})	Regional % of ANCP from DOP (%)
Northern	1	16.3	0.87	13.1	0.150	17.2
Indian	2	9.9	0.72	10.8	0.071	9.9
Southern	3	19.2	1.36	20.4	0.096	7.1
NPSG	4	12.5	0.95	14.3	0.198	20.8
EqPac	5	20.2	0.87	13.1	0.140	16.0
SPSG	6	11.0	0.71	10.6	0.149	21.0
NASG	7	10.3	0.56	8.4	0.064	11.5
EqAtl	8	14.8	0.20	3.0	0.015	7.7
SASG	9	14.7	0.43	6.5	0.039	9.0

3–5 mol C m^{-2} yr^{-1}. Minima in carbon-based ANCP rates are found within the subtropical gyres (regions 2, 4, 6, 7, and 9), the Arctic (region 1), and Southern Oceans in the range 0.04–1.5 mol C m^{-2} yr^{-1}. Intermediate ANCP rates (1.5–3 mol C m^{-2} yr^{-1}) are found within the midlatitude to subpolar regions of both hemispheres (regions 1 and 3) as well as across the equatorial regions (regions 5 and 8). The fraction of DOP-supported ANCP (i.e., μ[DOP]/ANCP) is presented in Figure 4c. Semilabile DOP contributes up to 80% of ANCP within the North Atlantic subtropical gyre with elevated contributions (~0.25–0.70) also found in the North Pacific and South Pacific subtropical gyres and the Arctic Oceans (region 1). Minima in DOP-supported ANCP (~0.02–0.10) are found within the Southern Ocean, midlatitude North Pacific and North Atlantic (region 1), Indian, South Atlantic subtropical gyre, and within upwelling systems (regions 1, 2, 5, and 8).

3.5. DOP Regeneration

The semilabile DOP remineralization flux (accumulating as DIP) from the net heterotrophic remineralization of DOP immediately below the productive layer is presented in Figure 5a. Regenerated semilabile DOP vertically integrated within the 73–279 m depth interval (model z layers 3–6) is maximal within the subarctic North Pacific and Atlantic as well as the Arctic (region 1), reaching values of ~5–10 mmol P m^{-2} yr^{-1} (Figure 5a). Intermediate values (~2.5–4 mmol P m^{-2} yr^{-1}) within this depth interval are found below the five subtropical gyre regions (regions 2, 4, 6, 7, and 9). Minima in regenerated semilabile DOP within the 73–279 m depth interval (<2 mmol P m^{-2} yr^{-1}) are found beneath the equatorial (regions 5 and 8) and eastern boundary upwelling systems (regions 1, 5, 7, and 9) as well as the Southern Ocean. The fraction of regenerated DIP within the 73–279 m depth interval attributable to semilabile DOP remineralization varies from ~0.1 to 0.8 (Figure 5b), with the remaining fraction arising from POP remineralization. Semilabile DOP remineralization makes its largest contribution to regenerated DIP within the 73–279 m layer beneath the five subtropical gyre regions (regions 2, 4, 6, 7, and 9) as well as the subpolar to polar latitudes of the northern hemisphere (region 1) with fractions in the range ~0.3–0.8. Of the five subtropical gyre regions, DOP regeneration makes its largest contribution in the North Atlantic followed by the North Pacific, the South Pacific and Indian, followed by the South Atlantic. The fractional contribution of semilabile DOP remineralization to DIP regeneration is at a minimum within the equatorial (regions 5 and 8) and eastern boundary upwelling regions (regions 1, 5, 7, and 9) as well as the Southern Ocean.

4. Discussion

4.1. Comparison of [DOP] Distributions to Prior Work

The OCIM P-cycling model [DOP] output presented here is the first global data product of DOP concentrations in which the biogeochemical cycle of DOP was the primary tracer optimized via data assimilation of marine DOP observations. The small mean bias of the OCIM P-cycling model [DOP] output, ~−4%, is an improvement over a prior effort involving a more complex biogeochemical model that included the coupled C, N, P, O_2, Fe, and Si

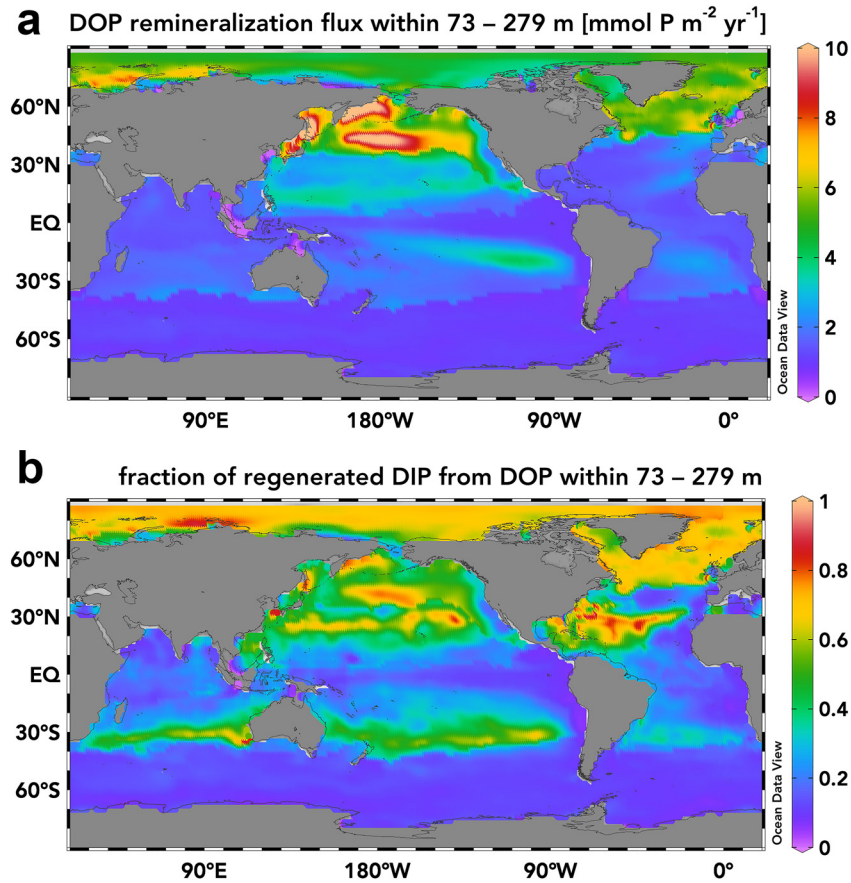

Figure 5. (a) Vertically integrated interior ocean dissolved organic phosphorus (DOP) remineralization flux accumulating as dissolved inorganic phosphorus (DIP) within the 73–279 m layer, mmol P m^{-2} yr^{-1}. (b) The fraction of regenerated DIP arising from DOP remineralization within the 73–279 m layer; remaining fraction arises from particulate organic phosphorus remineralization.

cycles (Letscher, Moore, et al., 2015), that achieved a mean [DOP] bias of ∼+7%. The correlation coefficient has also nearly doubled for model-observation pairs between studies, that is, from $r = 0.30$, $n = 2026$ (Letscher, Moore, et al., 2015) to $r = 0.54$, $n = 3{,}871$ in the current study. While the prior study did assimilate DOP concentration data to optimize marine DOM cycling, the representation of any particular tracer within the high complexity marine ecosystem-biogeochemical model employed in Letscher, Moore, et al. (2015) is subject to trade-offs in the necessity to jointly optimize dozens of biogeochemical tracers simultaneously. Likely also contributing to the observed improvement in representation of bulk [DOP] is the significant increase in the available DOP observations assimilated in the current study with the availability of the DOPv2021 database (Knapp et al., 2021) which contains double the open ocean [DOP] measurements. The largest difference between the surface ocean [DOP] distribution between the prior and new model data products is an overall near doubling of simulated [DOP] within more productive biomes of the world ocean (e.g., upwelling regions; regions 1, 5, 7, and 9), ∼0.4–0.5 μM (this study) versus ∼0.2–0.3 μM, and a near halving of simulated [DOP] within subtropical gyres (e.g., regions 2, 4, 6, 7, and 9), ∼0.05–0.1 μM (Figure 2, this study) versus ∼0.1–0.2 μM (Letscher, Moore, et al. (2015)). The simulated Indian Ocean surface [DOP] is ∼50% lower in the current study as compared to Letscher, Moore, et al. (2015), a region of the world ocean that continues to be undersampled for DOP. Seasonality could also play a role in generating biased simulated versus observed [DOP], as our model assumes steady state while the observations are inherently influenced by any local seasonal fluctuations in marine biogeochemistry. The DOPv2021 database contains ∼100–400 DOP concentration observations per month with a mean of ∼250/month, exhibiting limited seasonal biases in the data set assimilated in this study (Liang et al., in press). Additionally, Lomas et al. (2010) describe upper ocean DOP stocks at the BATS site in the North Atlantic subtropical gyre that vary

±20% over the seasonal cycle. We estimate that any unaccounted for seasonality in the model output of [DOP] and its related fluxes are on the order of <±20% with likely no one particular seasonal bias.

The OCIM P-cycling output provides the first global scale picture of the spatial distribution of surface ocean [DOP] that is validated against DOP observations from each of the major ocean basins afforded by the DOPv2021 observational database. Surface [DOP] is at a global minimum within the North Atlantic subtropical gyre as has been previously documented (Mather et al., 2008; Torres-Valdés et al., 2009); however, similar surface [DOP] depletions are observed for the other four subtropical gyre regions (Figure 2, regions 2, 4, 6, and 9). Surface [DOP] is elevated along the eastern flanks of the low latitude ocean basins and the equatorial ocean (regions 1, 5, and 7–9) as well as the subarctic North Pacific (region 1). These spatial patterns for surface [DOP] share a resemblance to that observed for surface ocean dissolved organic nitrogen concentrations [DON] (Letscher et al., 2013), which could be called that of "organic nutrients" (Letscher et al., 2016; Torres-Valdés et al., 2009). This spatial pattern for DON and DOP contrasts with that for dissolved organic carbon concentrations [DOC] in the surface ocean, which are known to exhibit regional maxima within the subtropical gyres resulting from the Ekman convergence of more recalcitrant DOC moieties in surface waters (Hansell, 2013; Hansell et al., 2009). Thus, for the organic nutrients, subtropical Ekman convergence supplies DON and DOP toward the oligotrophic gyres where a combination of heterotrophic and autotrophic consumption releases N and P from their organic macromolecules (e.g., Figure 3d), resulting in the observed sink of DON and DOP from surface waters across this gradient. For DOC, this same Ekman convergence contributes to the *accumulation* of surface [DOC] within the oligotrophic ocean, the difference perhaps reflecting the importance of organic nutrients in otherwise nutrient-impoverished gyres, and/or the more recalcitrant nature of DOC with respect to heterotrophic consumption in surface waters (Carlson et al., 2004; Letscher, Knapp, et al., 2015) as compared to DON and DOP (Figure 3, Hopkinson & Vallino, 2005; Letscher & Moore, 2015).

4.2. Spatial Patterns of Surface Ocean DOP Sources and Sinks

The spatial patterns of semilabile DOP production, autotrophic uptake, the fraction of euphotic zone DOP consumption attributed to autotrophs, and the resulting estimates of semilabile DOP lifetime within the upper ocean predicted by the OCIM P-cycling model are consistent with the role of DOP as an organic nutrient sustaining a portion of oligotrophic ocean productivity (Figure 3). The eastern tropical to subtropical Pacific (regions 1 and 5), the midlatitude and subarctic North Pacific (region 1), and to a lesser extent the eastern boundary upwelling systems and midlatitudes of the Atlantic (regions 1, 7, and 9) are identified as the biomes leading to the highest DOP production fluxes in the upper ocean, approaching 15–30 mmol P m^{-2} yr^{-1} (Figure 3a), which translate to elevated surface [DOP] (>0.3 μM) in the same regions (Figure 2). Iron stress when coupled with alleviated phosphorus stress are conditions that have been found to result in surface ocean DOP production and accumulation (Liang et al., 2022), which may help explain the elevated DOP production fluxes diagnosed for the subarctic North Pacific (region 1) and EqPac (region 5), although our model formulation only indirectly considers the role of iron on DOP fluxes through its impact on the satellite-diagnosed marine NPP rates. Conversely, the subtropical gyre regions of each basin (regions 2, 4, 6, 7, and 9) exhibit the lowest DOP production fluxes (Figure 3a) and lowered surface [DOP] (Figure 2) relative to neighboring biomes. This pattern, elevated DOP production along the equatorial, eastern, and midlatitude flanks of the subtropical gyres with depressed DOP production within the subtropical gyres, sets up a lateral gradient in surface ocean [DOP] which, when supplied toward the gyre centers by Ekman convergence, helps support a significant fraction of subtropical gyre NCP (this study, Letscher et al., 2016). In support of this, we computed the total combined lateral and vertical DOP transport convergence and divergence between regions, with respect to varying vertical horizons spanning the upper 73–556 m. The northern (region 1), southern (region 2), EqPac (region 5), and EqAtl (region 8) are identified as regions of net DOP transport divergence representing 14%–32%, 17%–36%, 14%–23%, and 1%–3% of the total global ocean DOP transport, respectively. The Indian (region 2), NPSG (region 4), SPSG (region 6), NASG (region 7), and SASG (region 9) are regions of net DOP convergence representing 1%–8%, 2%–17%, 0%–12%, 0%–3.5%, and 0%–3% of the total global ocean DOP transport, respectively.

Autotrophic uptake of semilabile DOP as a P-source sustaining new production was modeled following a reciprocal Monod function with observed PO_4^{3-} as the controlling factor. The minimum autotrophic uptake rate of semilabile DOP at elevated PO_4^{3-} concentrations was prescribed a value of 0.05 yr^{-1} (mean lifetime of 20 years) estimated from the existing literature of field-based alkaline phosphatase activities, the main enzyme used by

phytoplankton to access P from DOP substrates (Mather et al., 2008; Reynolds et al., 2014; Sato et al., 2013). The regionally resolved, most probable values of the half saturation constant, K_s (μM), governing the concentration of in situ PO_4^{3-} below which DOP uptake is stimulated, were found to cluster in the narrow range of 179–208 nM (Table 1). The resulting reciprocal Monod function (Equation 5), using parameters of $v = (20\ \text{yr})^{-1}$ and $K_s = \sim 200$ nM, yields an uptake curve in which autotrophic semilabile DOP uptake is $\mu = (10\ \text{yr})^{-1}$ when DIP = 200 nM, $\mu = (4\ \text{yr})^{-1}$ when DIP = 50 nM, and $\mu = (1\ \text{yr})^{-1}$ when DIP = 10 nM. An examination of the relationship between euphotic zone DIP and the fraction of DOP-supported ANCP in our model output reveals that the fraction of DOP-supported ANCP nearly doubles (~0.15 to ~0.30) between upper ocean DIP = 200–100 nM, with significant exponential increases in the DOP-supported ANCP below 100 nM DIP toward a fraction of unity. Combined, these results suggest that the niche for autotrophic DOP use as a P source sustaining growth is enhanced below a threshold of ~200 nM PO_4^{3-}, consistent with prior observations in gradients of alkaline phosphatase activities across the Atlantic (Mather et al., 2008) and eastern North Pacific (Dyhrman & Ruttenberg, 2006). However, surface ocean $[PO4]_{obs}$ is not the only factor determining autotrophic DOP uptake patterns, with the pattern of DOP production and its lateral transport away from source regions an important additional control. Autotrophic DOP uptake is greatest in the eastern Pacific (regions 1 and 5), reaching 6–8 mmol P m^{-2} yr^{-1} in the eastern tropical North Pacific and 4–5 mmol P m^{-2} yr^{-1} in the eastern tropical South Pacific (Figure 3b) coincident with and immediately "downstream" of the regions of greatest DOP production (Figure 3a). In general, autotrophic DOP uptake fluxes are moderately elevated (~2.5–4 mmol P m^{-2} yr^{-1}) within the regions immediately "downstream" in a surface current-flow sense, from equatorial and eastern boundary upwelling regions, as well as the neighboring midlatitudes along the equatorward, poleward, and eastern flanks of the subtropical gyres (Figure 3b). Enhanced autotrophic DOP uptake along gyre margins contributes to reduced estimates of the euphotic zone DOP lifetime within the subtropical ocean which are at their regional minima there, with lifetimes of ≤~1.25 yr (Figure 3c, regions 4, 6, 7, and 9). Autotrophic uptake of DOP outweighs heterotrophic DOP consumption nearly everywhere within the euphotic zone (Figure 3d) and is thus the primary control on DOP lifetime within the upper ocean (<73 m), especially within the subtropical gyres. Our model also predicts a strong contribution of autotrophic DOP uptake to DOP loss within surface waters of the Southern Ocean (Figure 3d), which is counterintuitive given this region's elevated PO_4^{3-}. Our estimates of autotrophic DOP uptake fluxes are low there, <2 mmol P m^{-2} yr^{-1}, as is the estimated heterotrophic DOP remineralization rate, lifetime = 9.7 years (Table 1). Thus, for comparisons of two fluxes of comparable magnitude, small changes in the estimates of either would have a large impact on their computed ratio, likely explaining our Southern Ocean result. DOP biogeochemistry is comparatively under studied within the Southern Ocean and could be targeted for future investigation.

4.3. Role for DOP in Support of ANCP

The OCIM P-cycling model presented here improves on earlier versions (e.g., Primeau et al., 2013; Teng et al., 2014; Wang et al., 2019) by assimilating DOP observational data to objectively constrain the regionally variable parameters governing its biogeochemical cycling. Thus, the resulting spatial pattern (Figure 4a) and globally integrated magnitude of the model estimated ANCP flux is the most consistent with the observed spatial patterns of PO_4^{3-} and DOP concentrations, satellite-estimated marine NPP rates (Westberry et al., 2008), and consideration of variable C:P stoichiometry in marine organic matter cycling. The globally integrated, P-based ANCP rate is estimated to be 5.4 Tmol P yr^{-1} (167.4 Tg P yr^{-1}). Carbon-based ANCP obtained from multiplication of P-based ANCP by the spatially variable $r_{C:P}$ stoichiometry of marine production based on in situ $[PO4]_{obs}$ (Galbraith & Martiny, 2015) yields an ANCP rate of 6.7 Pg C yr^{-1}. This places the OCIM P-cycling ANCP estimate within the lower end of the literature range of this globally important flux (5–14 Pg C yr^{-1}) computed from a range of methods (Emerson, 2014; Siegel et al., 2016). The Southern and Northern Oceans (regions 3 and 1) combined contribute approximately a third of this ANCP at a ratio of ~1.6:1, respectively (Table 2). The four subtropical gyres of the Pacific and Atlantic (regions 4, 6, 7, and 9) contribute ~40% of global ANCP at a Pacific:Atlantic basin ratio of ~1.6:1. The remaining ~27% of global ANCP occurs in the equatorial Pacific (region 5), equatorial Atlantic (region 8), and Indian Ocean (region 2). A notable bias is in the North Atlantic subtropical gyre where the OCIM P-cycling ANCP rates average ~0.5–1 mol C m^{-2} yr^{-1}, ~74%–87% lower than the mean of observational estimates, 3.8 ± 1.2 mol C m^{-2} yr^{-1} (summarized in Emerson, 2014). World Ocean Atlas PO_4^{3-} concentrations, which our model assimilates, are known to be biased high at locations with <200 nM observed PO_4^{3-} using high-sensitivity measurements (Martiny et al., 2019) such as the North Atlantic subtropical

gyre, contributing to a reduced vertical PO_4^{3-} gradient and thus associated supply to surface waters in our model, potentially explaining the low ANCP bias in our results.

Because the OCIM P-cycling model considers both DIP- and DOP-supported ANCP (Equations 1–3), it is possible to compute the fractional contribution of autotrophic semilabile DOP uptake to ANCP (Table 2). The resulting spatial pattern (Figure 4c) is largely consistent with that of an organic nutrient discussed above, with DOP supplying ∼0.1–0.8 of the P needed to sustain ANCP across the five subtropical gyres (regions 2, 4, 6, 7, and 9). Similar to previous estimates (Letscher et al., 2016; Torres-Valdés et al., 2009), DOP makes its largest fractional contribution to ANCP (0.3–0.8) within a region across the North Atlantic and North Pacific subtropical gyres between ∼15 and 30°N that is elevated toward the western half of each basin (Figure 4c). Similar elevated fractional contributions of DOP-supported ANCP are observed in the western subtropical South Pacific (region 6) and South Atlantic (region 9) and the Indian Ocean subtropical gyre (region 2), albeit at reduced levels, ∼0.1–0.3. Regionally averaged, DOP-supported ANCP rates range from 15 to 198 Tg C yr^{-1}, representing ∼7%–21% of overall ANCP in each region (Table 2). The largest DOP-supported contributions to regional ANCP, ∼21%, occur in the North and South Pacific subtropical gyres (regions 4 and 6). Elsewhere, autotrophic DOP uptake supports ∼7%–17% of regionally averaged ANCP. An interesting observation of our model result is that regions of elevated autotrophic DOP uptake fluxes (Figure 3b) do not exactly map onto the regions where DOP makes its largest fractional contribution to ANCP (Figure 4c). For example, the global maxima in autotrophic DOP uptake are found along the eastern boundary and across the midlatitudes to subarctic latitudes of the North Pacific Ocean (region 1), yet fractional contributions of DOP to ANCP are low to intermediate there, ∼0.1–0.2 (Figure 4c). Instead, fractional contributions of DOP-supported ANCP are elevated, ∼0.3–0.7, elsewhere in the North Pacific (region 4), within the adjacent subtropical gyre margins and gyre core. A similar pattern holds for the other five major ocean basins, albeit at varying levels of DOP-supported ANCP. Of note, the North Atlantic subtropical gyre exhibits intermediate rates of autotrophic DOP uptake, ∼1–3 mmol P m^{-2} yr^{-1}, yet the Sargasso Sea (region 7) harbors the global maximum in DOP-supported ANCP, ∼0.5–0.8. Our globally integrated, autotrophic uptake of DOP flux supplies ∼14% of marine export production, or ∼0.92 Pg C yr^{-1} of the total 6.67 Pg C yr^{-1} ANCP rate. Comparing the subtropical ocean gyre regions (regions 2, 4, 6, 7, and 9), estimates of the DOP-supported ANCP fraction are reduced ∼2%–30% by the OCIM P-cycling model as compared to an earlier study that used a high complexity, full marine ecosystem-biogeochemistry framework (Letscher et al., 2016). Estimates by the latter also included the fraction of ANCP supported indirectly by externally supplied DOP that is subsequently remineralized to PO_4^{3-} within the gyres, a flux that is not diagnosed in the present study, and which likely contributes to the lower estimates of DOP-supported ANCP.

4.4. Biogeochemical Impacts of DOP Remineralization

Because of its observed non-Redfield stoichiometry (Hopkinson & Vallino, 2005; Letscher & Moore, 2015), the fractional contribution of dissolved organic matter (DOM) to apparent oxygen utilization (AOU) within the ocean interior has long been of interest to estimate the spatiotemporal patterns of marine export production, nutrient cycling, and oxygen consumption more accurately (Abell et al., 2000; Carlson et al., 2010; Emerson, 2014; Fawcett et al., 2018; Hansell & Carlson, 2001; Hansell et al., 2009; Letscher & Villareal, 2018). At the global scale and assuming steady state, this fraction should match the fractional accumulation of ANCP as DOM, which for DOC has been estimated in the range ∼0.15–0.25 (Hansell et al., 2009; Letscher, Moore, et al., 2015; Romera-Castillo et al., 2016; Roshan & DeVries, 2017). However, this fraction is known to vary with both depth and biome across the ocean with typically higher contributions, ∼0.25–0.8, estimated for the shallower depth horizons (<500 m) beneath the subtropical gyre regions (Abell et al., 2000; Carlson et al., 2010; Hansell & Carlson, 2001; Letscher & Villareal, 2018; Roshan & DeVries, 2017). Here for semilabile DOP, its globally integrated fractional accumulation is estimated at 24.9% of ANCP with a matching fractional contribution to DIP regeneration below 73 m. We investigated the semilabile DOP remineralization flux within the shallow interior ocean (73–279 m) at depth horizons where DOM remineralization contributes most to AOU. Similar to previously identified spatial patterns for DOC remineralization, DOP remineralization between 73 and 279 m makes its largest fractional contribution to DIP regeneration beneath the subtropical gyre regions (regions 2, 4, 6, 7, and 9) as well as the subpolar and polar latitudes of the northern hemisphere (Figure 5b, region 1), in the range of ∼0.4–0.8. These locations correspond to regions of large-scale downwelling and/or minima in water mass "ideal age," estimated at a few years (DeVries & Deutsch, 2014). Considering the subtropical gyres, this shallow depth horizon (73–279 m) corresponds to isopycnal layers in the range σ_θ = ∼24.2–25.5 in the Pacific and σ_θ = ∼25.8–26.5 in the Atlantic

(Abell et al., 2000; Letscher & Villareal, 2018) which seasonally outcrop at the poleward edge of the gyres and/or immediately poleward within the midlatitudes (Letscher et al., 2013). These latitudes exhibit equatorward Ekman flow in the upper ocean, contributing to the subtropical Ekman convergence in each basin. Thus, regenerated DIP resulting from shallow remineralization of DOP in the subtropics that eventually returns to the surface near the poleward edge of the gyre is likely partially retained within the subtropical gyre system as surface ocean PO_4^{3-} and any DOP resulting from autotrophic production it supports is laterally advected toward the gyre centers. This shallow overturning loop between upper thermocline DOM remineralization near gyre centers and surface ocean lateral nutrient supply occurring near the gyre margins operating within the ocean subtropics has been suggested to be one mechanism by which marine nitrogen fixation (Abell et al., 2000), and NCP more generally, can be sustained over multiannual to decadal timescales (Letscher et al., 2016).

5. Final Comments

This work builds and improves on previous studies which have quantified the importance of autotrophic DOP uptake to contribute to ANCP regionally within the Atlantic basin (e.g., Torres-Valdés et al., 2009) and for the five subtropical gyre regions (Letscher et al., 2016), by providing the first global estimates of autotrophic DOP uptake (Figure 3b) and its fractional contribution to ANCP (Figure 4b). These global estimates are produced from an inverse model of marine P cycling that assimilated the largest data set of marine DOP observations to date, including global basin coverage. We note a spatial decoupling between regions where DOP supports the highest fraction of ANCP versus where the highest rates of autotrophic DOP consumption occur. Consistent with the earlier studies, the North Atlantic subtropical gyre (specifically, the Sargasso Sea) is identified as the region where autotrophic DOP uptake makes its largest fractional contribution to ANCP, consistent with the perennially low PO_4^{3-} concentrations and its vertical flux in this region (Lomas et al., 2010; Martiny et al., 2019). The North Pacific subtropical gyre is another region exhibiting elevated rates of autotrophic DOP utilization, consistent with previous work performed at Station ALOHA (Björkman & Karl, 2003). However, the model output predicts patterns of enhanced autotrophic DOP utilization with highest absolute rates immediately "downstream" of regions of net DOP production. This model prediction offers opportunities for validation by future field studies, including within the subtropical South Pacific, tropical Pacific, the Indo-Pacific throughflow region, and the western Arctic Ocean. Furthermore, the model predicts minima in autotrophic DOP utilization within recently upwelled waters, the midlatitude recirculation regions of the surface western boundary currents (e.g., Gulf Stream, Kuroshio), the Southern Ocean, and the Indian Ocean. The latter two regions as well as the Arctic continue to suffer from poor data coverage for DOP which could be targeted for future research. Finally, recent work has identified a potentially important role for the availability of dissolved iron (Fe) and/or ecosystem Fe stress in determining the biogeochemical context in which marine DOP accumulates or is utilized as an additional autotrophic P source within surface waters (Liang et al., 2022). The OCIM P-cycling model presented here does not explicitly model the linkages between the marine P and Fe cycles; however, Fe limitation, as well as nitrogen and/or light stress, is implicitly included in the formulation of the autotrophic DIP uptake term that is a spatially variable function based on the pattern of marine NPP (γ term, Equation 4). Many marine diazotrophs are known to obtain a disproportionately large fraction of their cellular P demand from DOP (Mulholland et al., 2002; Orchard, Benitez-Nelson, et al., 2010; Sohm & Capone, 2006) and are often colimited by Fe (Kustka et al., 2002; Mills et al., 2004). Future modeling work could aim to explicitly couple the marine P and Fe cycles to investigate the nexus of iron and DOP supply with diazotrophy contributing to marine ANCP.

Data Availability Statement

The recent global compilation of [DOP] measurements (the DOPv2021 database v2) is available either at the Biological and Chemical Data Management Office (BCO-DMO) (https://www.bco-dmo.org/dataset/855139) or in the Woods Hole Open Access Server (https://doi.org/10.26008/1912/bco-dmo.855139.2), under a Creative Commons Attribution 4.0 license. The World Ocean Atlas 2013 v2 PO_4^{3-} data are available the National Centers for Environmental Information (NOAA), https://doi.org/10.7289/V5NZ85MT, under a public domain license. Model code is available at GitHub, https://github.com/rletscher/GBC_DOP_Letscher, under a GNU General Public License.

Acknowledgments
We thank all the scientists, crew, and analysts involved with the production of the marine dissolved organic phosphorus concentration database that made this work possible. Additionally, we appreciate the constructive feedback received during review. This work was supported by NSF OCE #1829916 (R.T.L.) and NSF OCE #1829797 (A.N.K. and Z.L.).

References

Abell, J., Emerson, S., & Renaud, P. (2000). Distributions of TOP, TON and TOC in the North Pacific subtropical gyre: Implications for nutrient supply in the surface ocean and remineralization in the upper thermocline. *Journal of Marine Research*, *58*(2), 203–222. https://doi.org/10.1357/002224000321511142

Ammerman, J. W., Hood, R. R., Case, D. A., & Cotner, J. B. (2003). Phosphorus deficiency in the Atlantic: An emerging paradigm in oceanography. *Eos, Transactions American Geophysical Union*, *84*(18), 165–170. https://doi.org/10.1029/2003eo180001

Behrenfeld, M. J., Boss, E., Siegel, D. A., & Shea, D. M. (2005). Carbon-based ocean productivity and phytoplankton physiology from space. *Global Biogeochemical Cycles*, *19*(1), GB1006. https://doi.org/10.1029/2004gb002299

Behrenfeld, M. J., & Falkowski, P. G. (1997). Photosynthetic rates derived from satellite-based chlorophyll concentration. *Limnology and Oceanography*, *42*(1), 1–20. https://doi.org/10.4319/lo.1997.42.1.0001

Björkman, K. M., & Karl, D. M. (2003). Bioavailability of dissolved organic phosphorus in the euphotic zone at Station ALOHA, North Pacific Subtropical Gyre. *Limnology and Oceanography*, *48*(3), 1049–1057. https://doi.org/10.4319/lo.2003.48.3.1049

Carlson, C. A., Giovannoni, S. J., Hansell, D. A., Goldberg, S. J., Parsons, R., & Vergin, K. (2004). Interactions among dissolved organic carbon, microbial processes, and community structure in the mesopelagic zone of the northwestern Sargasso Sea. *Limnology and Oceanography*, *49*(4), 1073–1083. https://doi.org/10.4319/lo.2004.49.4.1073

Carlson, C. A., Hansell, D. A., Nelson, N. B., Siegel, D. A., Smethie, W. M., Khatiwala, S., et al. (2010). Dissolved organic carbon export and subsequent remineralization in the mesopelagic and bathypelagic realms of the North Atlantic basin. *Deep Sea Research Part II: Topical Studies in Oceanography*, *57*(16), 1433–1445. https://doi.org/10.1016/j.dsr2.2010.02.013

Casey, J. R., Lomas, M. W., Michelou, V. K., Dyhrman, S. T., Orchard, E. D., Ammerman, J. W., & Sylvan, J. B. (2009). Phytoplankton taxon-specific orthophosphate (Pi) and ATP utilization in the western subtropical North Atlantic. *Aquatic Microbial Ecology*, *58*(1), 31–44. https://doi.org/10.3354/ame01348

Charria, G., Dadou, I., Llido, J., Drevillon, M., & Garcon, V. (2008). Importance of dissolved organic nitrogen in the north Atlantic Ocean in sustaining primary production: A 3-D modelling approach. *Biogeosciences*, *5*(5), 1437–1455. https://doi.org/10.5194/bg-5-1437-2008

DeVries, T., & Deutsch, C. (2014). Large-scale variations in the stoichiometry of marine organic matter respiration. *Nature Geoscience*, *7*(12), 890–894. https://doi.org/10.1038/ngeo2300

DeVries, T., Deutsch, C., Rafter, P. A., & Primeau, F. (2013). Marine denitrification rates determined from a global 3-D inverse model. *Biogeosciences*, *10*(4), 2481–2496. https://doi.org/10.5194/bg-10-2481-2013

DeVries, T., & Holzer, M. (2019). Radiocarbon and helium isotope constraints on deep ocean ventilation and mantle-3He sources. *Journal of Geophysical Research: Oceans*, *124*(5), 3036–3057. https://doi.org/10.1029/2018jc014716

Diaz, J. M., Holland, A., Sanders, J. G., Bulski, K., Mollett, D., Chou, C. W., et al. (2018). Dissolved organic phosphorus utilization by phytoplankton reveals preferential degradation of polyphosphates over phosphomonoesters. *Frontiers in Marine Science*, *5*, 380. https://doi.org/10.3389/fmars.2018.00380

Dugdale, R. C., & Goering, J. J. (1967). Uptake of new and regenerated forms of nitrogen in primary productivity 1. *Limnology and Oceanography*, *12*(2), 196–206. https://doi.org/10.4319/lo.1967.12.2.0196

Duhamel, S., Diaz, J. M., Adams, J. C., Djaoudi, K., Steck, V., & Waggoner, E. M. (2021). Phosphorus as an integral component of global marine biogeochemistry. *Nature Geoscience*, *14*(6), 359–368. https://doi.org/10.1038/s41561-021-00755-8

Dyhrman, S. T., Chappell, P. D., Haley, S. T., Moffett, J. W., Orchard, E. D., Waterbury, J. B., & Webb, E. A. (2006). Phosphonate utilization by the globally important marine diazotroph Trichodesmium. *Nature*, *439*(7072), 68–71.

Dyhrman, S. T., & Ruttenberg, K. C. (2006). Presence and regulation of alkaline phosphatase activity in eukaryotic phytoplankton from the coastal ocean: Implications for dissolved organic phosphorus remineralization. *Limnology and Oceanography*, *51*(3), 1381–1390. https://doi.org/10.4319/lo.2006.51.3.1381

Emerson, S. (2014). Annual net community production and the biological carbon flux in the ocean. *Global Biogeochemical Cycles*, *28*(1), 14–28. https://doi.org/10.1002/2013gb004680

Eppley, R. W., Garside, C., Renger, E. H., & Orellana, E. (1990). Variability of nitrate concentration in nitrogen-depleted subtropical surface waters. *Marine Biology*, *107*(1), 53–60. https://doi.org/10.1007/bf01313241

Eppley, R. W., & Peterson, B. J. (1979). Particulate organic matter flux and planktonic new production in the deep ocean. *Nature*, *282*(5740), 677–680. https://doi.org/10.1038/282677a0

Fawcett, S. E., Johnson, K. S., Riser, S. C., Van Oostende, N., & Sigman, D. M. (2018). Low-nutrient organic matter in the Sargasso Sea thermocline: A hypothesis for its role, identity, and carbon cycle implications. *Marine Chemistry*, *207*, 108–123. https://doi.org/10.1016/j.marchem.2018.10.008

Galbraith, E. D., & Martiny, A. C. (2015). A simple nutrient-dependence mechanism for predicting the stoichiometry of marine ecosystems. *Proceedings of the National Academy of Sciences of the United States of America*, *112*(27), 8199–8204. https://doi.org/10.1073/pnas.1423917112

Garcia, H. E., Locarnini, R. A., Boyer, T. P., Antonov, J. I., Baranova, O. K., Zweng, M. M., et al. (2013). World ocean atlas 2013. Volume 4: Dissolved inorganic nutrients (phosphate, nitrate, silicate). https://doi.org/10.7289/V5J67DWD

Gruber, N., Keeling, C. D., & Stocker, T. F. (1998). Carbon-13 constraints on the seasonal inorganic carbon budget at the BATS site in the northwestern Sargasso Sea. *Deep Sea Research Part I: Oceanographic Research Papers*, *45*(4–5), 673–717. https://doi.org/10.1016/s0967-0637(97)00098-8

Hansell, D. A. (2013). Recalcitrant dissolved organic carbon fractions. *Annual Review of Marine Science*, *5*(1), 421–445. https://doi.org/10.1146/annurev-marine-120710-100757

Hansell, D. A., & Carlson, C. A. (2001). Biogeochemistry of total organic carbon and nitrogen in the Sargasso Sea: Control by convective overturn. *Deep Sea Research Part II: Topical Studies in Oceanography*, *48*(8–9), 1649–1667. https://doi.org/10.1016/s0967-0645(00)00153-3

Hansell, D. A., Carlson, C. A., Repeta, D. J., & Schlitzer, R. (2009). Dissolved organic matter in the ocean: A controversy stimulates new insights. *Oceanography*, *22*(4), 202–211. https://doi.org/10.5670/oceanog.2009.109

Hashihama, F., Saito, H., Shiozaki, T., Ehama, M., Suwa, S., Sugiyama, T., et al. (2020). Biogeochemical controls of particulate phosphorus distribution across the oligotrophic subtropical Pacific Ocean. *Global Biogeochemical Cycles*, *34*(9), e2020GB006669. https://doi.org/10.1029/2020gb006669

Hopkinson, C. S., & Vallino, J. J. (2005). Efficient export of carbon to the deep ocean through dissolved organic matter. *Nature*, *433*(7022), 142–145. https://doi.org/10.1038/nature03191

John, S. G., Liang, H., Weber, T., DeVries, T., Primeau, F., Moore, K., et al. (2020). AWESOME OCIM: A simple, flexible, and powerful tool for modeling elemental cycling in the oceans. *Chemical Geology*, *533*, 119403. https://doi.org/10.1016/j.chemgeo.2019.119403

Johnson, K. S., Riser, S. C., & Karl, D. M. (2010). Nitrate supply from deep to near-surface waters of the North Pacific subtropical gyre. *Nature*, *465*(7301), 1062–1065. https://doi.org/10.1038/nature09170

Karl, D. M., & Björkman, K. M. (2015). Dynamics of dissolved organic phosphorus. In *Biogeochemistry of marine dissolved organic matter* (pp. 233–334). Academic Press.

Keeling, C. D., Brix, H., & Gruber, N. (2004). Seasonal and long-term dynamics of the upper ocean carbon cycle at Station ALOHA near Hawaii. *Global Biogeochemical Cycles*, *18*(4), GB4006. https://doi.org/10.1029/2004gb002227

Knapp, A. N., Letscher, R. T., & Liang, Z. (2021). *DOP concentration observations from the global ocean between 1990 and 2021(DOPv2021)*. Biological and Chemical Oceanography Data Management Office, v1. https://doi.org/10.26008/1912/bco-dmo.855139.1

Kustka, A., Carpenter, E. J., & Sañudo-Wilhelmy, S. A. (2002). Iron and marine nitrogen fixation: Progress and future directions. *Research in Microbiology*, *153*(5), 255–262. https://doi.org/10.1016/s0923-2508(02)01325-6

Lanpher, K. B., & Popendorf, K. J. (2021). Variability of microbial particulate ATP concentrations in subeuphotic microbes due to underlying metabolic strategies in the South Pacific Ocean. *Frontiers in Marine Science*, *8*, 603. https://doi.org/10.3389/fmars.2021.655898

Letscher, R. T., Hansell, D. A., Carlson, C. A., Lumpkin, R., & Knapp, A. N. (2013). Dissolved organic nitrogen in the global surface ocean: Distribution and fate. *Global Biogeochemical Cycles*, *27*(1), 141–153. https://doi.org/10.1029/2012gb004449

Letscher, R. T., Knapp, A. N., James, A. K., Carlson, C. A., Santoro, A. E., & Hansell, D. A. (2015). Microbial community composition and nitrogen availability influence DOC remineralization in the South Pacific Gyre. *Marine Chemistry*, *177*, 325–334. https://doi.org/10.1016/j.marchem.2015.06.024

Letscher, R. T., & Moore, J. K. (2015). Preferential remineralization of dissolved organic phosphorus and non-Redfield DOM dynamics in the global ocean: Impacts on marine productivity, nitrogen fixation, and carbon export. *Global Biogeochemical Cycles*, *29*(3), 325–340. https://doi.org/10.1002/2014gb004904

Letscher, R. T., Moore, J. K., Teng, Y. C., & Primeau, F. (2015). Variable C: N: P stoichiometry of dissolved organic matter cycling in the Community Earth System Model. *Biogeosciences*, *12*(1), 209–221. https://doi.org/10.5194/bg-12-209-2015

Letscher, R. T., Primeau, F., & Moore, J. K. (2016). Nutrient budgets in the subtropical ocean gyres dominated by lateral transport. *Nature Geoscience*, *9*(11), 815–819. https://doi.org/10.1038/ngeo2812

Letscher, R. T., & Villareal, T. A. (2018). Evaluation of the seasonal formation of subsurface negative preformed nitrate anomalies in the subtropical North Pacific and North Atlantic. *Biogeosciences*, *15*(21), 6461–6480. https://doi.org/10.5194/bg-15-6461-2018

Li, T., Guo, C., Zhang, Y., Wang, C., Lin, X., & Lin, S. (2018). Identification and expression analysis of an atypical alkaline phosphatase in *Emiliania huxleyi*. *Frontiers in Microbiology*, *9*, 2156. https://doi.org/10.3389/fmicb.2018.02156

Liang, Z., Letscher, R. T., & Knapp, A. N. (2022). Dissolved organic phosphorus concentrations in the surface ocean controlled by both phosphate and iron stress. *Nature Geoscience*, *15*(8), 651–657. https://doi.org/10.1038/s41561-022-00988-1

Liang, Z., McCabe, K., Fawcett, S. E., Forrer, H. J., Jeandel, C., Marconi, D., et al. (in press). A global ocean dissolved organic phosphorus concentration database (DOPv2021). *Scientific Data*. https://doi.org/10.1038/s41597-022-01873-7

Lin, H. Y., Shih, C. Y., Liu, H. C., Chang, J., Chen, Y. L., Chen, Y. R., et al. (2013). Identification and characterization of an extracellular alkaline phosphatase in the marine diatom Phaeodactylum tricornutum. *Marine Biotechnology*, *15*(4), 425–436. https://doi.org/10.1007/s10126-013-9494-3

Lomas, M. W., Burke, A. L., Lomas, D. A., Bell, D. W., Shen, C., Dyhrman, S. T., & Ammerman, J. W. (2010). Sargasso Sea phosphorus biogeochemistry: An important role for dissolved organic phosphorus (DOP). *Biogeosciences*, *7*(2), 695–710. https://doi.org/10.5194/bg-7-695-2010

Martin, J. H., Knauer, G. A., Karl, D. M., & Broenkow, W. W. (1987). VERTEX: Carbon cycling in the northeast Pacific. *Deep-Sea Research, Part A: Oceanographic Research Papers*, *34*(2), 267–285. https://doi.org/10.1016/0198-0149(87)90086-0

Martin, P., Dyhrman, S. T., Lomas, M. W., Poulton, N. J., & Van Mooy, B. A. (2014). Accumulation and enhanced cycling of polyphosphate by Sargasso Sea plankton in response to low phosphorus. *Proceedings of the National Academy of Sciences of the United States of America*, *111*(22), 8089–8094. https://doi.org/10.1073/pnas.1321719111

Martiny, A. C., Lomas, M. W., Fu, W., Boyd, P. W., Yuh-ling, L. C., Cutter, G. A., et al. (2019). Biogeochemical controls of surface ocean phosphate. *Science Advances*, *5*(8), eaax0341. https://doi.org/10.1126/sciadv.aax0341

Mather, R. L., Reynolds, S. E., Wolff, G. A., Williams, R. G., Torres-Valdes, S., Woodward, E. M. S., et al. (2008). Phosphorus cycling in the North and South Atlantic Ocean subtropical gyres. *Nature Geoscience*, *1*(7), 439–443. https://doi.org/10.1038/ngeo232

Michaels, A. F., Bates, N. R., Buesseler, K. O., Carlson, C. A., & Knap, A. H. (1994). Carbon-cycle imbalances in the Sargasso Sea. *Nature*, *372*(6506), 537–540. https://doi.org/10.1038/372537a0

Mills, M. M., Ridame, C., Davey, M., La Roche, J., & Geider, R. J. (2004). Iron and phosphorus co-limit nitrogen fixation in the eastern tropical North Atlantic. *Nature*, *429*(6989), 292–294. https://doi.org/10.1038/nature02550

Moutin, T., Karl, D. M., Duhamel, S., Rimmelin, P., Raimbault, P., Van Mooy, B. A., & Claustre, H. (2008). Phosphate availability and the ultimate control of new nitrogen input by nitrogen fixation in the tropical Pacific Ocean. *Biogeosciences*, *5*(1), 95–109. https://doi.org/10.5194/bg-5-95-2008

Mulholland, M. R., Floge, S., Carpenter, E. J., & Capone, D. G. (2002). Phosphorus dynamics in cultures and natural populations of Trichodesmium spp. *Marine Ecology Progress Series*, *239*, 45–55. https://doi.org/10.3354/meps239045

Orchard, E. D., Ammerman, J. W., Lomas, M. W., & Dyhrman, S. T. (2010). Dissolved inorganic and organic phosphorus uptake in Trichodesmium and the microbial community: The importance of phosphorus ester in the Sargasso Sea. *Limnology and Oceanography*, *55*(3), 1390–1399. https://doi.org/10.4319/lo.2010.55.3.1390

Orchard, E. D., Benitez-Nelson, C. R., Pellechia, P. J., Lomas, M. W., & Dyhrman, S. T. (2010). Polyphosphate in trichodesmium from the low-phosphorus Sargasso Sea. *Limnology and Oceanography*, *55*(5), 2161–2169. https://doi.org/10.4319/lo.2010.55.5.2161

Primeau, F. W., Holzer, M., & DeVries, T. (2013). Southern Ocean nutrient trapping and the efficiency of the biological pump. *Journal of Geophysical Research: Oceans*, *118*(5), 2547–2564. https://doi.org/10.1002/jgrc.20181

Reynolds, S., Mahaffey, C., Roussenov, V., & Williams, R. G. (2014). Evidence for production and lateral transport of dissolved organic phosphorus in the eastern subtropical North Atlantic. *Global Biogeochemical Cycles*, *28*(8), 805–824. https://doi.org/10.1002/2013gb004801

Romera-Castillo, C., Letscher, R. T., & Hansell, D. A. (2016). New nutrients exert fundamental control on dissolved organic carbon accumulation in the surface Atlantic Ocean. *Proceedings of the National Academy of Sciences of the United States of America*, *113*(38), 10497–10502. https://doi.org/10.1073/pnas.1605344113

Roshan, S., & DeVries, T. (2017). Efficient dissolved organic carbon production and export in the oligotrophic ocean. *Nature Communications*, *8*(1), 1–8. https://doi.org/10.1038/s41467-017-02227-3

Roussenov, V., Williams, R. G., Mahaffey, C., & Wolff, G. A. (2006). Does the transport of dissolved organic nutrients affect export production in the Atlantic Ocean? *Global Biogeochemical Cycles*, *20*(3), GB3002. https://doi.org/10.1029/2005gb002510

Sato, M., Sakuraba, R., & Hashihama, F. (2013). Phosphate monoesterase and diesterase activities in the North and South Pacific Ocean. *Biogeosciences*, *10*(11), 7677–7688. https://doi.org/10.5194/bg-10-7677-2013

Shaked, Y., Xu, Y., Leblanc, K., & Morel, F. M. (2006). Zinc availability and alkaline phosphatase activity in Emiliania huxleyi: Implications for Zn-P co-limitation in the ocean. *Limnology and Oceanography*, *51*(1), 299–309. https://doi.org/10.4319/lo.2006.51.1.0299

Siegel, D. A., Buesseler, K. O., Behrenfeld, M. J., Benitez-Nelson, C. R., Boss, E., Brzezinski, M. A., et al. (2016). Prediction of the export and fate of global ocean net primary production: The EXPORTS science plan. *Frontiers in Marine Science*, *3*, 22. https://doi.org/10.3389/fmars.2016.00022

Sohm, J. A., & Capone, D. G. (2006). Phosphorus dynamics of the tropical and subtropical north Atlantic: Trichodesmium spp. versus bulk plankton. *Marine Ecology Progress Series*, *317*, 21–28. https://doi.org/10.3354/meps317021

Su, Z., Olman, V., & Xu, Y. (2007). Computational prediction of Pho regulons in cyanobacteria. *BMC Genomics*, *8*(1), 1–12. https://doi.org/10.1186/1471-2164-8-156

Teng, Y. C., Primeau, F. W., Moore, J. K., Lomas, M. W., & Martiny, A. C. (2014). Global-scale variations of the ratios of carbon to phosphorus in exported marine organic matter. *Nature Geoscience*, *7*(12), 895–898. https://doi.org/10.1038/ngeo2303

Torres-Valdés, S., Roussenov, V. M., Sanders, R., Reynolds, S., Pan, X., Mather, R., et al. (2009). Distribution of dissolved organic nutrients and their effect on export production over the Atlantic Ocean. *Global Biogeochemical Cycles*, *23*(4), GB4019. https://doi.org/10.1029/2008gb003389

Wang, W. L., Moore, J. K., Martiny, A. C., & Primeau, F. W. (2019). Convergent estimates of marine nitrogen fixation. *Nature*, *566*(7743), 205–211. https://doi.org/10.1038/s41586-019-0911-2

Weber, T., Cram, J. A., Leung, S. W., DeVries, T., & Deutsch, C. (2016). Deep ocean nutrients imply large latitudinal variation in particle transfer efficiency. *Proceedings of the National Academy of Sciences of the United States of America*, *113*(31), 8606–8611. https://doi.org/10.1073/pnas.1604414113

Westberry, T., Behrenfeld, M. J., Siegel, D. A., & Boss, E. (2008). Carbon-based primary productivity modeling with vertically resolved photoacclimation. *Global Biogeochemical Cycles*, *22*(2), GB2024. https://doi.org/10.1029/2007gb003078

Wu, J., Sunda, W., Boyle, E. A., & Karl, D. M. (2000). Phosphate depletion in the western North Atlantic Ocean. *Science*, *289*(5480), 759–762. https://doi.org/10.1126/science.289.5480.759

Yoshimura, T., Nishioka, J., Saito, H., Takeda, S., Tsuda, A., & Wells, M. L. (2007). Distributions of particulate and dissolved organic and inorganic phosphorus in North Pacific surface waters. *Marine Chemistry*, *103*(1–2), 112–121. https://doi.org/10.1016/j.marchem.2006.06.011